

Article

A Study on the Mechanical Characteristics and Wheel–Rail Contact Simulation of a Welded Joint for a Large Radio Telescope Azimuth Track

Xiao Chen ¹, Ruihua Yin ¹, Zaitun Yang ¹, Huiqing Lan ^{1,*}  and Qian Xu ^{2,3}

¹ Key Laboratory of Vehicle Advanced Manufacturing, Measuring and Control Technology (Ministry of Education), Beijing Jiaotong University, Beijing 100044, China; 21125985@bjtu.edu.cn (X.C.); 23121388@bjtu.edu.cn (R.Y.); 22125985@bjtu.edu.cn (Z.Y.)

² Xinjiang Astronomical Observation, Chinese Academy of Sciences, Urumqi 830001, China; xuqian@xao.ac.cn

³ Key Laboratory of Radio Astronomy, Chinese Academy of Sciences, Urumqi 830011, China

* Correspondence: hqlan@bjtu.edu.cn

Abstract: The azimuth track is an important component of the radio telescope wheel–rail system. During operation, the azimuth track is inevitably subject to phenomena such as track wear, track fatigue cracks, and impact damage to welded joints, which can affect observation accuracy. The 110 m QiTai radio telescope (QTT) studied in this paper is the world’s largest fully steerable radio telescope at present, and its track will bear the largest load ever. Since the welded joint of an azimuth track is the weakest part, an innovative welding method (multi-layer and multi-pass weld) is adopted for the thick welding section. Therefore, it is necessary to study the contact mechanical properties between the wheel and the azimuth track in this welded joint. In this study, tensile tests based on digital image correlation technology (DIC) and Vickers hardness tests are carried out in the metal zone (BM), heat-affected zone (HAZ), modified layer, and weld zone (WZ) of the welded joint, and the measured data are used to fit the elastic–plastic constitutive model for the different zones of the welded joint in the azimuth track. Based on the constitutive model established, a nonlinear finite element model is built and used to simulate the rolling mechanical performance between the wheel and azimuth track. Through the analysis of simulated data, we obtained the stress distribution of the track under different pre-designed loads and identified the locations most susceptible to damage during ordinary working conditions, braking conditions, and start-up conditions. The result can provide a significant theoretical basis for future research and for the monitoring of large track damage.

Keywords: azimuth track; welded joint; multi-layer and multi-pass; wheel–rail contact; mechanical property; finite element model



Citation: Chen, X.; Yin, R.; Yang, Z.; Lan, H.; Xu, Q. A Study on the Mechanical Characteristics and Wheel–Rail Contact Simulation of a Welded Joint for a Large Radio Telescope Azimuth Track. *Buildings* **2024**, *14*, 1300. <https://doi.org/10.3390/buildings14051300>

Academic Editors: Atsushi Suzuki and Dinil Pushpalal

Received: 7 April 2024

Revised: 30 April 2024

Accepted: 2 May 2024

Published: 5 May 2024



Copyright: © 2024 by the authors. Licensee MDPI, Basel, Switzerland. This article is an open access article distributed under the terms and conditions of the Creative Commons Attribution (CC BY) license (<https://creativecommons.org/licenses/by/4.0/>).

1. Introduction

During the operation of radio telescopes, a series of problems affecting the pointing accuracy of the azimuth tracks [1], such as track wear, fatigue cracks, and impact damage to track welded joints, occur in the wheel–rail contact system. A lot of design optimizations and improvements to tracks have already been conducted [2–4]. For the QiTai radio telescope (QTT) studied in this paper, the joints of the azimuth track are all welded. Since the welded joint is the weakest part of the entire track, most of the damage occurs in this zone. The welded joint of the azimuth track adopts an innovative multi-pass welding method of multi-layer and multi-pass due to the thick track. Therefore, it is significant to study the contact mechanical characteristics in the welded joint.

In the research of welded joints, there are four methods commonly used to obtain the local mechanical properties. The first method is based on hardness testing, characterizing the local constitutive behavior of the welded joint by the correlation between hardness values and strength, but the empirical hardness–strength relationship proposed

by different researchers is only valid for the materials studied and lacks universality. The second method is to obtain the stress–strain constitutive relationship by cutting microscopic specimens and conducting tensile, shear, and impact tests. This method can provide a relatively accurate stress–strain constitutive relationship as long as the material in the specimen is uniform. However, it is difficult to ensure the uniformity of the material in the joint due to the presence of welding heat, especially in the heat-affected zone where material property gradients exist. The third method is to simulate the welding process through thermodynamic finite element analysis, but it is difficult to accurately reproduce the temperature history of the welded joint. The fourth method is the DIC technology approach. This method has made good progress. According to these methods, many scholars have conducted all kinds of experiments. Microscopically, Kumar et al. [5] conducted micro-hardness, tensile, and impact tests on the welded joints and analyzed the microstructural properties of the multi-pass welded joints. Han [6] explained the evolution of the microstructure and mechanical properties of welded joints. These studies focused on the microstructure of materials and achieved good results. Macroscopically, Saranath et al. [7] conducted research on the welded joints by cutting microscopic samples and subjecting them to tension, shear, and impact tests, but it is difficult to ensure the uniformity of the materials due to the influence of thermal processes in the welded joint. Zhang et al. [8] studied the welded joints by simulating the weld process through thermodynamic finite element analysis, but it is difficult to accurately reproduce the temperature history of the welded joint. However, with the widespread application of digital image correlation (DIC) technology, the aforementioned problems have been solved. Zhang et al. [9] used DIC technology to analyze the strain field of the welded joint, which can effectively obtain the local constitutive relation of the nonuniform welded joint, but it also has a drawback in that it cannot obtain the complete stress–strain curve of the nonfracture position.

In the research on wheel–rail contact, there are already a sufficient theoretical foundation and technical methods for determining the wheel–rail contact of track vehicles. For the mechanical analysis and damage analysis of wheel–rail contact, the mainstream methods currently are finite element simulation analysis and numerical simulation analysis. Tan and Shi [10] used numerical simulation to solve wheel–rail fatigue damage. Moreover, they [11] also used the multi-finite-element coupling method and the multi-time-step solution method to solve the dynamics of wheel–rail contact. Many wheel–rail contact methods have been applied in azimuth tracks such as the finite element method. Arslan [12] and Twllsikivi [13] found that the track is more prone to significant plastic deformation during wheel–rail contact. Kuminek and Aniolek [14] investigated the influence of computational accuracy. Tian et al. [15] analyzed the deformation patterns during wheel–rail contact. Fu et al. [16] obtained the maximum contact stress and contact width of the wheel–rail based on the Hertz elastic contact theory. Yang et al. [17] discussed wheel–rail frictional rolling contact using the explicit finite element analysis method. However, these methods lack an experimental basis for material parameters, material properties, and track division. Moreover, the models established above are finite element models of the form “base metal–welded joint–base metal”. Although this method saves a lot of computation time, it ignores the influence of the heat-affected zone of the welded joint, leading to significant discrepancies between the simulation results and the actual test results.

In this paper, we conducted experiments at a macro level. We combined and improved existing methods to analyze the welded joint of the azimuth track by conducting tensile tests and Vickers hardness measurements based on digital image technology. Then, we fitted constitutive models of the welded joint by comparing and analyzing the experimental data, and a real finite element model of the azimuth track was established. Based on these, the Mises stress of welded joints during smooth operation under different loads and the distribution of stress on the welded joint surface during start-up and braking conditions were obtained by simulation.

2. Experiment

2.1. Tensile Experiment Based on DIC

The test material was selected from the 110 m radio telescope overall track weld sample provided by 39th Research Institute of China Electronics Technology Group Corporation. The track material is 42CrMo steel and adopts a method of multi-pass, single-groove welding for the track. The welding process first implements the welding of the modified layer, followed by the welding of the filling layer, and finally implements the welding of the surface overlay layer. Figure 1 shows the overall track weld sample and joint form of the 110 m radio telescope.

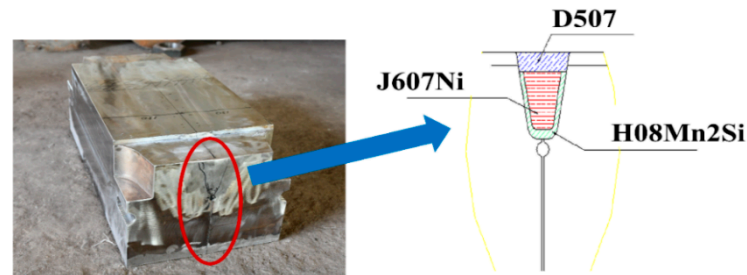


Figure 1. A 110 m radio telescope overall azimuth track weld sample and joint form.

According to the tensile test method for metallic materials in ISO 6892-1:2019 [18], a quasi-static tensile specimen was cut and designed at the welded joint of the 110 m radio azimuth track using wire electrical discharge machining. Considering the use of a layered weld process for the azimuth track welded joint, a cut was carried out along the depth direction of the welded joint based on the weld morphology. There were two types of test specimens, namely specimen 1 and specimen 2. They both consisted of the metal zone (BM), the heat-affected zone (HAZ), the modified layer, and the weld zone (WZ), but the difference between them was that they use different weld methods for the WZ. The dumbbell specimen was sampled longitudinally along the track. The sampling position and the physical object are shown in Figure 2.

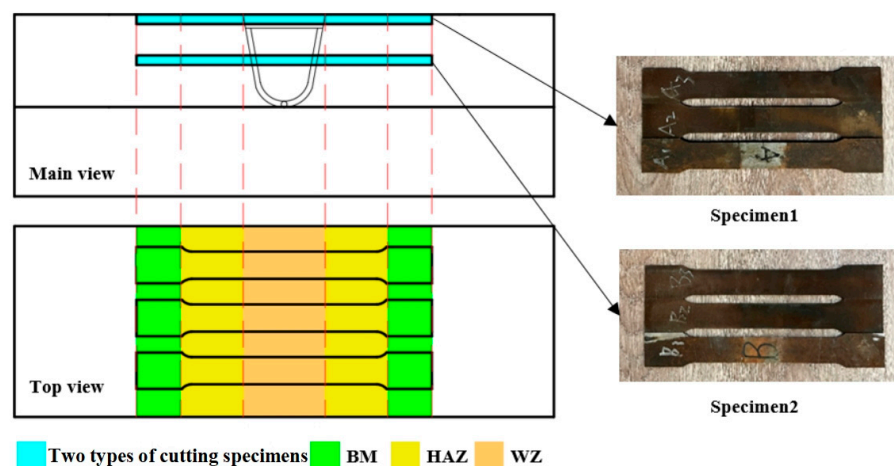


Figure 2. Schematic diagram of specimen sampling location.

The uniaxial tensile test was conducted on an INSTRON 5982 composite material testing machine and a VIC-3D measurement system, as shown in Figure 3a. The stretching experiment machine uses displacement control. The VIC-3D strain measurement system includes two highly integrated high-speed cameras that can track the displacement and strain of each pixel within the field of view. They were placed at an angle of 30° approximately in front of the specimen to capture the speckle changes on the surface of the specimen during the stretching process. DIC technology can obtain the strain of any point on the

predetermined path at any time. The optical measurement points mainly serve as virtual extensometers to measure the strain distribution at the ROI zone of the welded joint. The optical measurement path combined with the stretching sample is shown in Figure 3b, with an optical measurement range of 160 mm, including the BM, HAZ, and WZ.

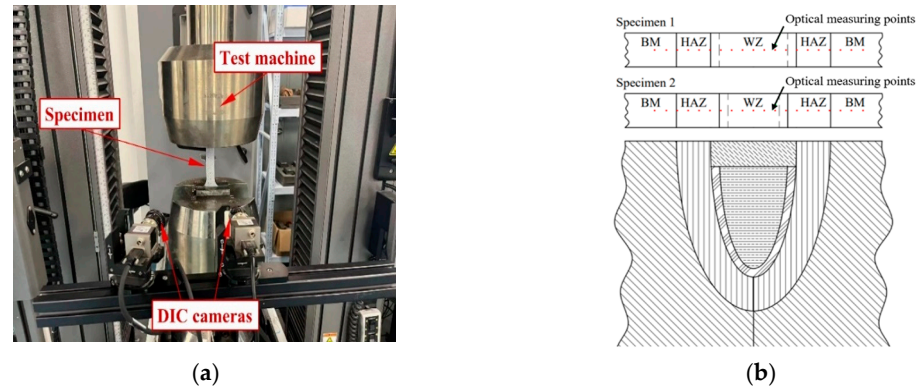


Figure 3. Tensile test with DIC. (a) Test measurement equipment; (b) schematic diagram of the location of optical measurement points.

2.2. Hardness Experiment

According to standard ISO 6507-1:2005 [19], the Vickers hardness test was conducted on the welded joint, as shown in Figure 4a. In this test, a small force was applied perpendicular to the test surface for Vickers hardness, with a maximum loading time of 8 s and a head descent speed not exceeding 0.3 mm/s. The lengths of the two diagonal lines of the indentation were measured, and the Vickers hardness value was calculated according to the relevant standard. As shown in Figure 4b, the hardness measurement was centered on the welded joint, spanning four zones from position A to B, namely the WZ, the modified layer, the HAZ, and the BM. The total length of AB was approximately 75 mm, with a spacing of 5 mm, and a total of 16 hardness points were tested. The test force was 0.98 N, with a duration of 8 s. To improve the accuracy of the hardness test and eliminate anomalies, the welded joint underwent three hardness tests, and the average value was taken as the final result of the Vickers hardness test for that welded joint.



Figure 4. Hardness test. (a) Instrument for Vickers hardness test; (b) schematic diagram of the location of Vickers hardness measurement points.

2.3. Experimental Results and Data Analysis

Figure 5 shows the strain contours of the welded joint DIC at different times. It can be seen that the strain distribution on both sides of the WZ remained symmetrical. In specimen 1, the strain was mainly concentrated in the HAZ, with smaller strain values in the BM and WZ. As the load increased, necking occurred in the HAZ. In specimen 2, the strain was also concentrated in the zone close to the welded joint, namely the HAZ and the modified layer zone, while the strain in the BM and WZ remained relatively stable. With the increase in load, a fracture occurred in the HAZ position.

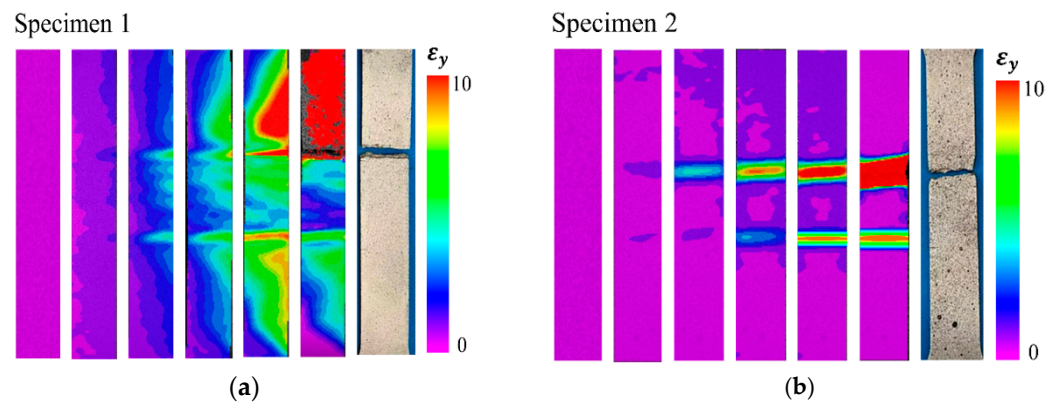


Figure 5. The strain contours of specimens. (a) Specimen 1; (b) specimen 2.

From Figure 6, it can be seen that only the HAZ and the modified layer exhibited relatively complete stress–strain curves, indicating that, the weaker the mechanical performance of the stress–strain parameters, the more prone the weld is to fracture. Additionally, the weld material showed significant heterogeneity, with noticeable differences in the mechanical performance of the BM, HAZ, overlay layer, modified layer, and filler layer.

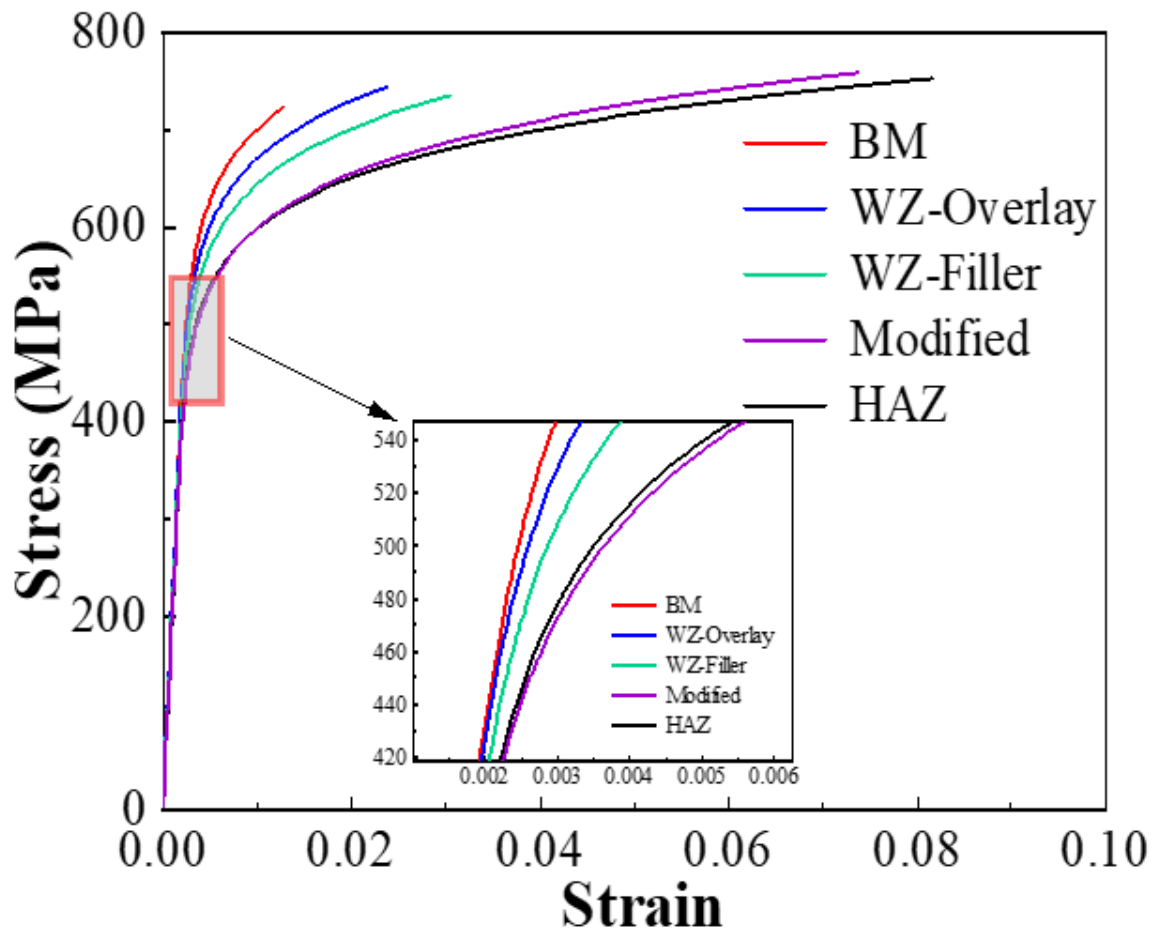


Figure 6. Stress–strain curve of welded joints.

The characteristic points were extracted from the BM, HAZ, overlay layer, modified layer, and filler layer. The strain–time curves of each zone’s characteristic points were plotted on the same graph, as shown in Figure 7. It can be seen that the strain rate of the HAZ and the modified layer was significantly higher than that of the overlay and the BM. As the time increased, the changes in strain in the HAZ were most evident.

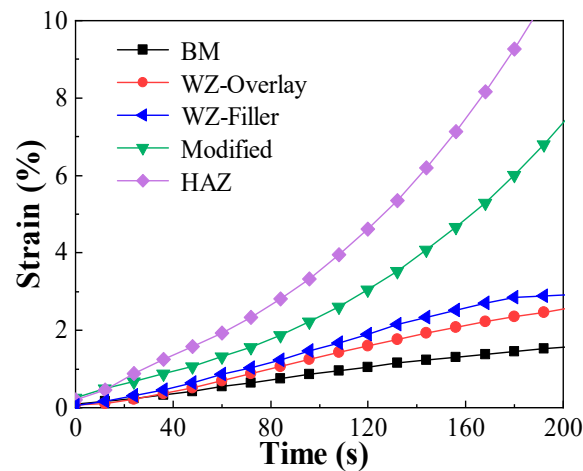


Figure 7. Strain–time variation curve.

Figure 8 shows the distribution curve of strain on the surface of the welded joint under different tensile loads. It can be observed that, as the tensile load increased, the strain distribution on the surface of the welded joint exhibited approximately symmetrical characteristics with respect to the WZ. In addition, the strain variation in the BM and WZ was relatively small, while it was more significant in the HAZ.

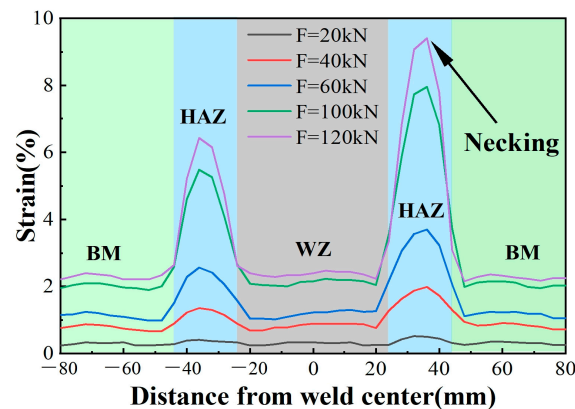


Figure 8. Changes in strain of welded joints under different loads.

From Figure 9, it can be seen that the distribution pattern of the elastic modulus in the welded joint showed a W-shaped distribution. The elastic modulus of the BM was the highest, followed by the WZ, and the HAZ and the modified layer had the lowest elastic modulus. This can explain the reason why plastic deformation first occurred at the HAZ and modified layer in the DIC strain contour. Figure 10 shows the distribution pattern of yield strength in the welded joint: The order of magnitude for the yield strength and tensile strength of specimen 1 was BM > WZ-Overlay > modified layer > HAZ. The yield strength of specimen 2 was in the following order: BM > WZ-Filler > modified layer > HAZ. Although the HAZ and the modified layer were more prone to plastic deformation, their elongation after fracture was higher than that for the BM and WZ.

Figure 11 shows that the hardness of the WZ-Overlay of specimen 1 fluctuated within the range of 310 HV to 340 HV, while the hardness of the BM fluctuated in the range 325 HV~375 HV; the minimum hardness of the welded joint was located at the HAZ. As the distance from the center of the welded joint increased, the hardness of the welded joint gradually decreased. At a distance of 35 mm from the center of the welded joint, there was a low hardness point, with hardness values fluctuating in the range of 200 HV~225 HV. The hardness of the WZ-Filler in specimen 2 fluctuated in the range of 300 HV~337 HV, and the

hardness of the BM fluctuated in the range of 325 HV~375 HV. The minimum hardness of the welded joint was located at the HAZ.

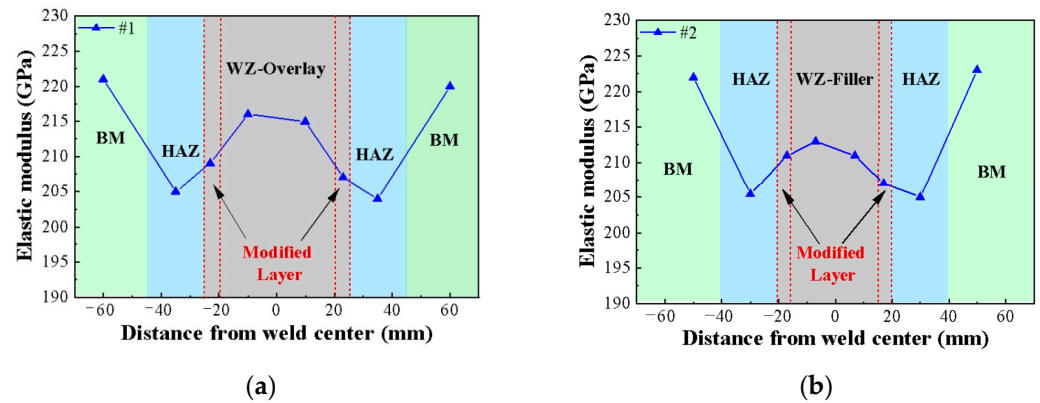


Figure 9. Elastic modulus contours of specimens. (a) Sample 1; (b) Sample 2.

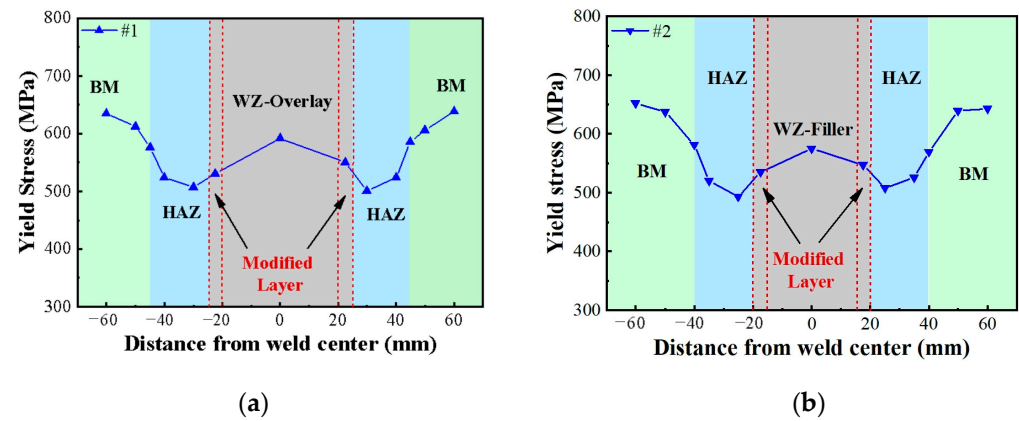


Figure 10. The yield stress contours of specimens. (a) Sample 1; (b) Sample 2.

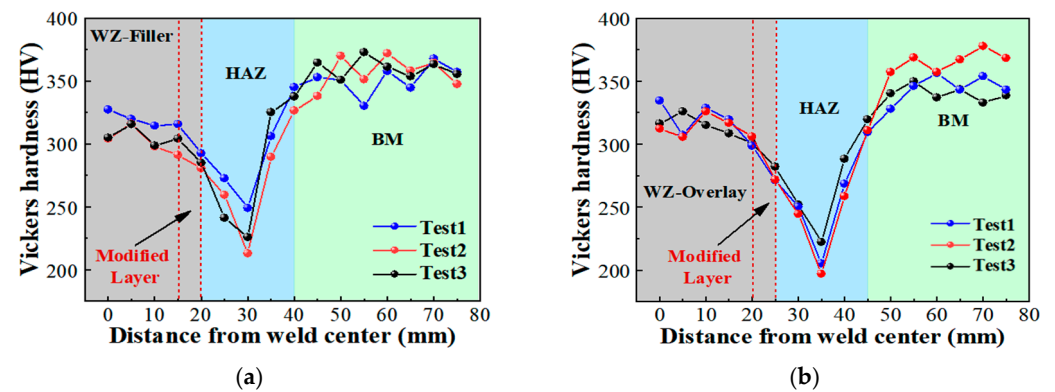


Figure 11. The Vickers hardness contours of specimens. (a) Sample 1; (b) Sample 2.

The hardness values of WZ and BM changed relatively little, while the hardness of HAZ fluctuated greatly. This is because the HAZ undergoes heating and cooling cycles, which cause changes in its microstructure and properties. The most severe change is grain growth, which leads to the most significant softening and affects the hardness value. As the distance from the center of the welded joint increases, the influence of heat input weakens, and the hardness gradually recovers to the BM, which determines that the weakest zone of the welded joint is located at the HAZ.

Figure 12 compares the distribution of Vickers hardness and yield strength in the welded joint, it was found that there was a certain correlation between them. Similarly, the hardness value fluctuated significantly at the HAZ.

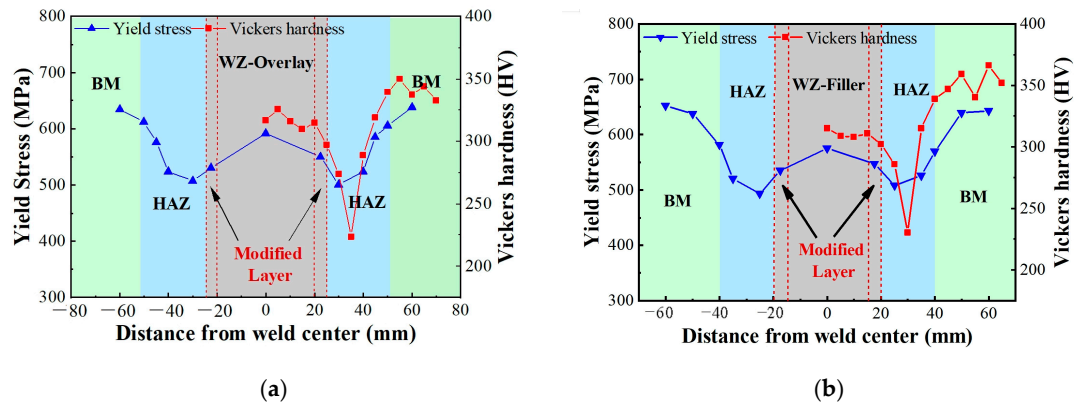


Figure 12. Yield stress and Vickers hardness contours of specimens. (a) Sample 1; (b) Sample 2.

3. Model

3.1. Elastic–Plastic Constitutive Model

From the mechanical curves, it is known that there are differences in the mechanical properties of the BM, HAZ, and WZ, and their strain relationships all exhibited significant nonlinear characteristics. Therefore, the use of linear elastic models or bilinear constitutive models cannot accurately describe the hardening of the welded joint.

The Ramberg–Osgood model [20], as an excellent method for fitting material characteristic curves considering strain hardening effects, is widely used to establish and describe the elastic–plastic and the stress–strain relationships of metal materials. This model was initially proposed by C. G. Ramberg and W. R. Osgood in 1943. The basic form of the model is as follows:

$$\varepsilon = \frac{\sigma}{E} + \varepsilon_0 \left(\frac{\sigma}{\sigma_{\varepsilon_0}} \right)^n \quad (1)$$

where E is the elastic modulus, σ_{ε_0} is the conventional elastic limit, ε is the residual strain corresponding to σ_{ε_0} , and n is the strain hardening parameter.

As shown in Figure 6, it can be seen from the experimental curve that both the base material and the weld material did not have a clear yield. Therefore, the constitutive parameters of the R-O constitutive relationship fitting model were chosen. The stress at 0.2% plastic strain was taken as the conventional elastic limit.

$$\sigma_{\varepsilon_0} = \sigma_{0.2} \quad (2)$$

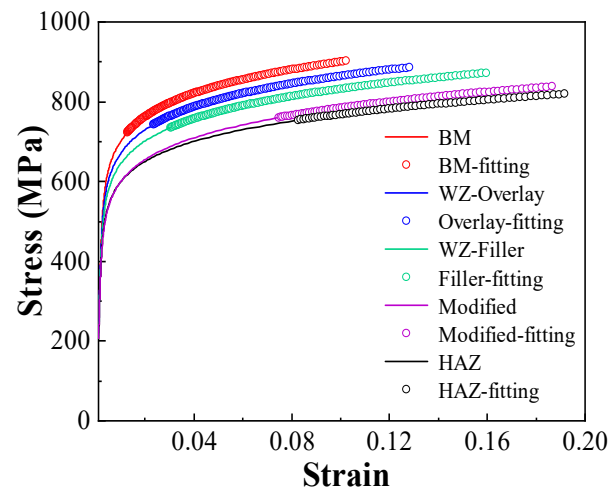
Correspondingly, if $\sigma_{\varepsilon_0} = 0.002$, the equation can be transformed into the following:

$$\varepsilon = \frac{\sigma}{E} + 0.002 \left(\frac{\sigma}{\sigma_{0.2}} \right)^n \quad (3)$$

Equation (3) represents the stress–strain constitutive equation of the track welded joint under uniaxial tensile load. By conducting uniaxial tensile tests, the nominal stress–strain curves of each zone’s optical measurement points were obtained. After converting them into true stress–strain curves, we can obtain the elastic modulus and yield limit of the material. Further fitting the experimental data using the R-O constitutive model yields the strain hardening exponent, thus completing the determination of the material’s R-O constitutive parameters. The constitutive parameters are shown in Table 1 and the comparison between the experiment and the fitting model is given in Figure 13. It shows that the R-O fitting model was a good fit.

Table 1. Constitutive parameters of welded joint material for azimuth track.

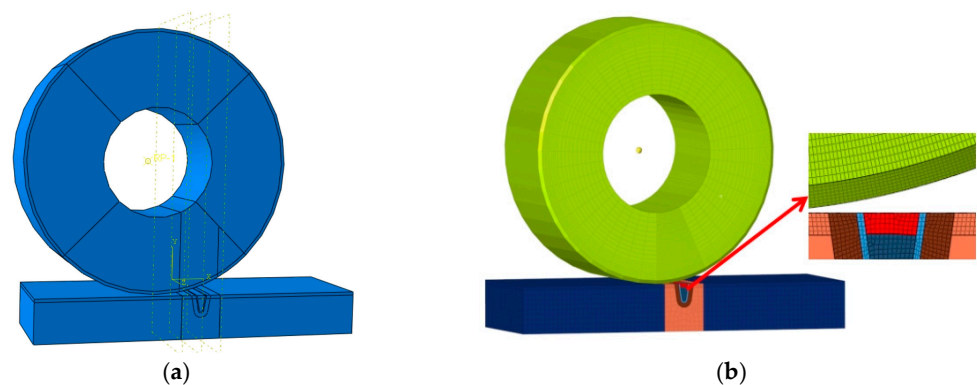
Zone	E/GPa	$\sigma_{0.2}/MPa$	n
BM	221	623.7	10.55
HAZ	205	530.6	9.469
WZ-Modified	207	542.2	9.672
WZ-Overlay	215	594.6	10.16
WZ-Filler	212	574.8	10.245

**Figure 13.** Experimental stress–strain curve and fitting.

3.2. Finite Element Model

3.2.1. Structure and Mesh

A simulation model of the track welded joint was built with five parts: BM, HAZ, WZ-Modified layer, WZ-Overlay, and WZ-Filler. Figure 14a shows the different material properties assigned to the five parts for subsequent simulation analysis. Based on the results of the mechanical experiment, the width of the welded joint on the track surface was 50 mm, with a depth of 80 mm. The ends of the welded joint were closely attached to the BM, with a transition layer width of 5 mm. The width of the overlay layer on the top of the welded joint was 15 mm, with the center part being the filler layer, and the width of the HAZ was 20 mm. The material properties were set as 42CrMo for the track and wheel base material, H08Mn2Si for the modified layer, D507 for the surfacing layer, and J607Ni for the filling layer, with specific plastic parameters obtained from the experiments.

**Figure 14.** Wheel-track model. (a) Solid model, (b) Finite element model.

To ensure calculation accuracy, hexahedral elements were used for discretization of the antenna track, wheel, and welding area in the model, and C3D8R elements suitable for contact calculation were selected. Compared to regular fully integrated elements, one

integration point was reduced in each direction. Linear reduced integration elements have only one integration point at the center of the element, making it easy to view the analysis results at the integration point. Figure 14b shows the local mesh refinement in the welding seam area and the wheel–rail contact area.

3.2.2. Boundary Conditions

To simulate fixed boundary conditions, all degrees of freedom of the bottom nodes of the track were constrained. The contact properties between the wheel and the track can be divided into normal action and tangential action. For normal action, the system defaulted to using a “hard contact” model, where the contact pressure between contact surfaces can reach infinity, and the gap can be a negative value. As for tangential action, the system used the Coulomb friction model to describe the friction characteristics between contact surfaces, where the friction coefficient is used to measure the resistance of the contact surfaces in the tangential direction.

3.2.3. Stress Initialization

There were three steps for the analysis. The purpose of the first analysis step was to move the wheel downwards to make it come into contact with the track with an interference fit, thus establishing a stable contact between the track and the wheel. The purpose of the second analysis step was to release gravity to allow the wheel track to naturally establish steady contact. The purpose of the third analysis step was to establish steady rolling of the wheel. Figure 15 shows the cross distribution of contact stress on the track surface after steady rolling.

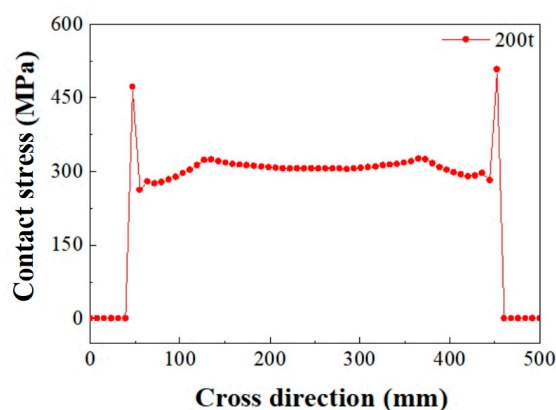


Figure 15. Contact stress distribution on the surface of track.

The purpose of the second analysis step was to apply gravity to make the wheel press down and rebound on the track, ultimately establishing a stable natural contact state between the wheel and the track. This process is to gradually reduce the gap between the wheel and the track, achieving a tighter wheel–rail contact effect. As shown in Figure 16, it can be seen that as the incremental step increased, the contact stress fluctuated violently before 0.4 s, repeatedly pressing down and rebounding. The stress will increase when pressed down and decrease when rebounding. Finally, after 0.4 s, the contact stress of the track gradually tended to a constant value, indicating that a steady contact state between the wheel and track was established at this time.

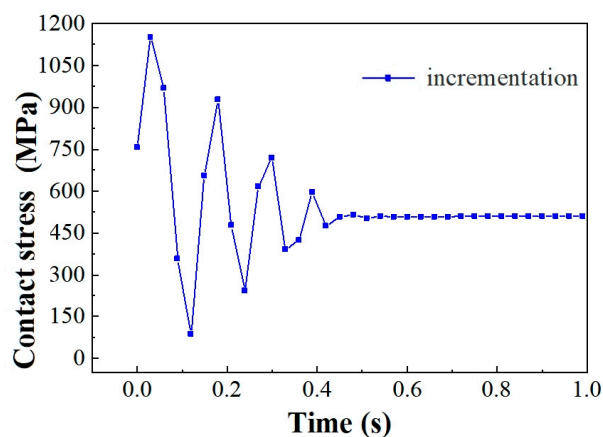


Figure 16. Curve of contact stress with analysis step time.

4. Simulation and Discussion

4.1. The Mises Stress of Welded Joints during Ordinary Working Condition under Different Loads

The overall weight of the QTT is about 6000–7000 tons. It is supported by approximately 30 or more bearing wheels, with each wheel bearing a load of about 200–240 tons. In order to study the influence of the self-weight of the structure on the mechanical characteristics of the azimuth wheel–rail rolling contact, a simulation study for ordinary working condition was conducted to examine the variation in contact stress under five different loads: 200 t, 210 t, 220 t, 230 t, and 240 t.

Figure 17a–c shows the contour of Mises stress under partial loads at different depths of the azimuth track in the BM, HAZ, and WZ. Extracting the Mises stress along the depth direction, the trend of the Mises stress in the BM, HAZ, and WZ with different loads can be obtained in Figure 17d–f. It can be seen that the Mises stress showed a trend of increasing first and then decreasing with the change in the contact surface depth, and the values of the Mises stress all reached the maximum at a subsurface depth of about 6 mm on the contact surface. For example, the Mises contour under 210 t at 6 mm depth in the HAZ was 375.2 MPa, and it was obviously higher than that at other depths in the same conditions.

Figure 18a shows a stress contour example of the Mises stress distribution in the BM under 200 t. Figure 18b shows the situation of the maximum Mises stress in the different zones under different loads. It can be observed that the Mises stress on the wheel–rail gradually increased with the increase in load. Meanwhile, it also showed a trend of the stress field with “HAZ > WZ > BM”; it was fully and completely consistent with the distribution pattern of yield strength in the experiment. Figure 19 shows the vertical deformation distribution of the azimuth track welding joints under different loads, with the vertical deformation of the HAZ being the largest, followed by the WZ, and that of the BM being the smallest.

Through simulation analysis in this part, we first predicted the overall stress field distribution of the QTT under the ordinary working condition with different pre-loads, and this verified the correctness of the experiment by the distribution of the stress in each zone. Secondly, the zone with the highest stress was located at 25–27 mm on both sides of the center of the weld in the track welding area, while the areas with lower stress were at 0–24 mm on both sides and 50 mm away. Thirdly, it was found that the most perilous points for the future operation of the QTT were 22 mm inward from both sides of the cross track and 6 mm vertically from the track. Finally, it was concluded that the maximum vertical deformation occurred in the HAZ zone when the design axle load was 230 t.

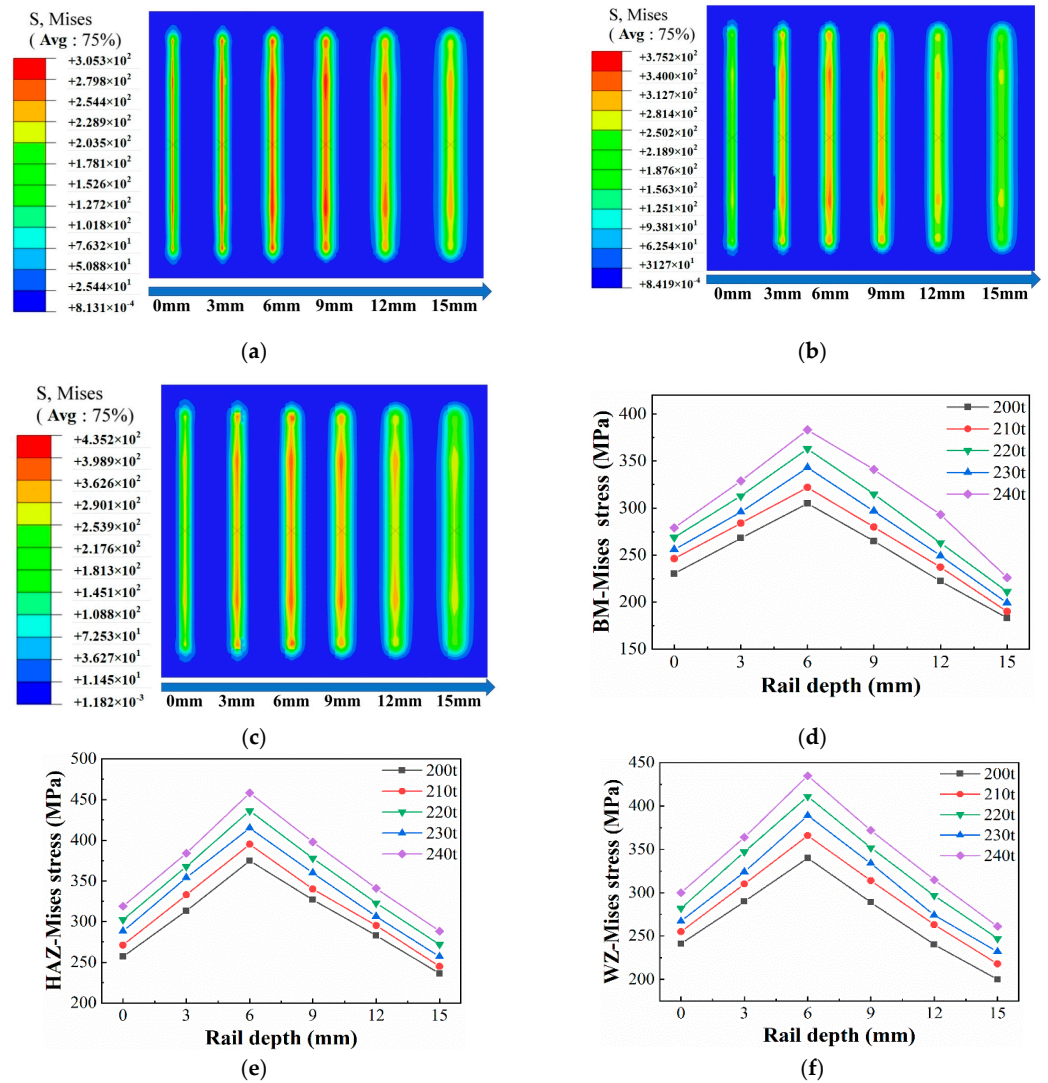


Figure 17. Mises stress distribution in the weld zone at different depths. (a) Mises contour under 200 t at different depths in the BM; (b) Mises contour under 210 t at different depths in the HAZ; (c) Mises contour under 240 t at different depths in the WZ; (d) Mises contour under different loads at different depths in the BM; (e) Mises contour under different loads at different depths in the HAZ; (f) Mises contour under different loads at different depths in the WZ.

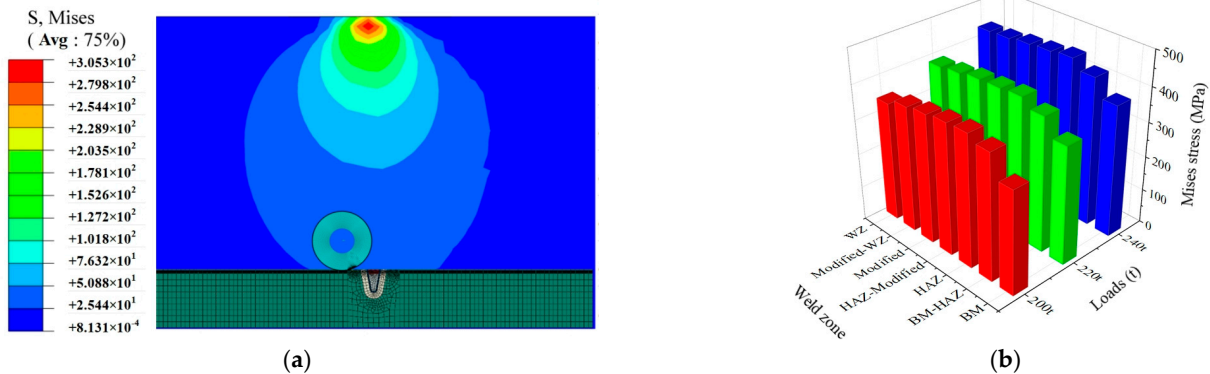


Figure 18. Mises stress distribution in the weld zone under different loads. (a) Mises stress distribution in the BM under 200 t. (b) Mises stress distribution in the welded joint under different loads.

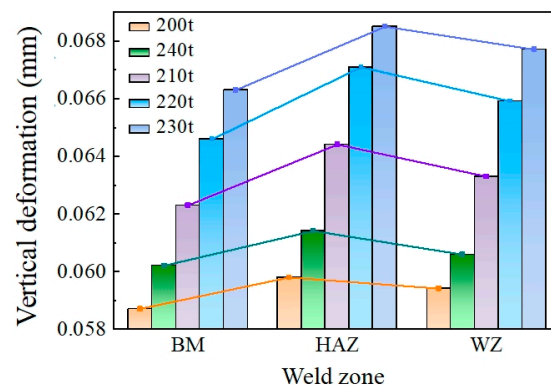


Figure 19. Vertical deformation distribution of weld zone under different loads.

4.2. Formatting of Mathematical Components

This section conducts finite element simulations of the start-up and rapid braking of the large radio telescope to better understand the force conditions on the track. Based on the results, appropriate measures can be taken, such as limiting acceleration and velocity, to reduce damage to the track and ensure its safety and reliability.

4.2.1. Start-Up Working Condition

Simulation analysis of the mechanical response of the welded joint at various zones during the telescope start-up process under a 200 t load. The start-up speed is defined using the smooth step amplitude curve provided in ABAQUS, with an acceleration to 1 rad/s within 1 s. The start-up speed loading method is shown in Figure 20a.

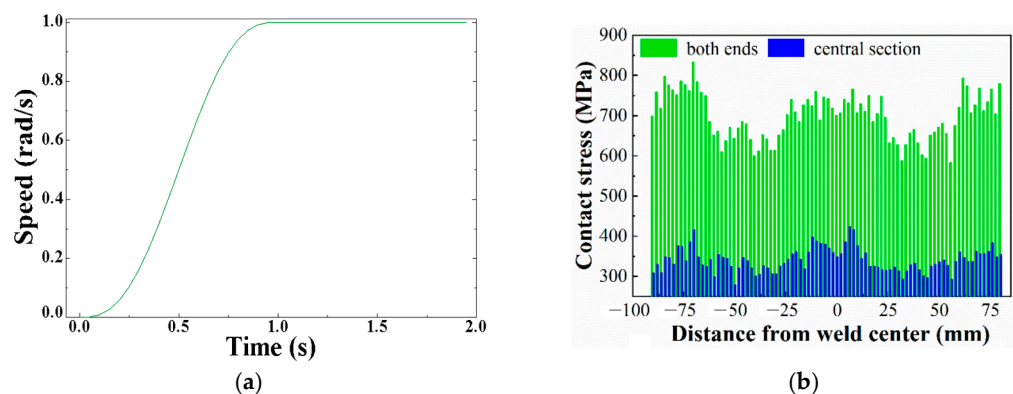


Figure 20. Start-up condition. (a) Speed loading method; (b) distribution of contact stress on the surface of the welded joint.

Figure 20b depicts the contact stress distribution on the surface of the welded joint under start-up conditions. It can be observed that the BM, HAZ, and WZ exhibited significant differences in contact stress, and there was also considerable fluctuation in the distribution of contact stress values within the same zone. However, the stress in each zone fluctuated within a fixed range. From a global perspective, under the operating conditions, the distribution of contact stress on the surface of the welded joint showed a W-like pattern.

Therefore, it can be seen that the contact stress amplification in the HAZ was the highest among the three different zones. This indicates that the start-up condition has the greatest impact on the contact stress of the HAZ, which may have a significant effect on the durability of the joint.

4.2.2. Braking Condition

To test the braking condition, we simulated the mechanical response of the welded joint in different zones under a 200 t load during the rapid braking process. In the rapid

braking condition, the smooth step amplitude curve provided by ABAQUS was used to define the braking process, as shown in Figure 21a, and it was set to decelerate to 0 rad/s within 1 s.

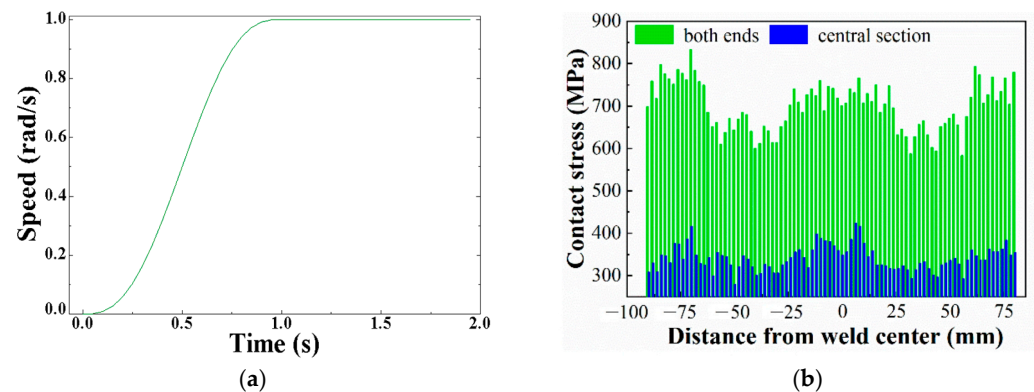


Figure 21. Braking condition. (a) Speed loading method; (b) distribution of contact stress on welded joint surface.

According to Figure 21b, the contact stress distribution on the surface of the welded joint under braking conditions also showed a W-shaped distribution.

Under the start-up condition, the average contact stress at both ends of the BM contact area was approximately 750 MPa, while the average contact stress in the middle of the contact area was approximately 460 MPa; the average contact stress at both ends of the HAZ contact area was approximately 630 MPa, with the average stress in the middle of the contact area at approximately 430 MPa; the average contact stress at both ends of the WZ contact area was approximately 720 MPa, with the average stress in the middle of the contact area at approximately 450 MPa. A comparison with the mechanical parameters of the joint under steady conditions in the previous section revealed that the contact stress in the rail joint area under the start-up conditions was significantly higher than that under stable contact conditions. Specifically, in the HAZ contact area, the contact stress at both ends and in the middle increased by 161 MPa and 102 MPa. It can be seen that, among the three different areas, the HAZ contact area experienced the greatest increase in contact stress. This indicates that the start-up has the greatest impact on the contact stress of the HAZ, which may have a significant impact on the durability of the joint. Therefore, greater attention should be paid to the health of the HAZ. Meanwhile, compared to the distribution of contact stress on the surface of the welded joint in the start-up condition, the braking condition had a similar trend, and its HAZ was also weak.

5. Conclusions

This article experimentally investigated the position distribution and mechanical properties of the BM, HAZ, modified layer, overlay layer, and filling layer in the welded joint of a large azimuth track for the first time through the combination of image recognition with tensile and Vickers hardness tests macroscopically and explored the stress–strain relationship in each region.

By obtaining the tensile curve, image recognition strain field, Vickers hardness curve, and distribution of yield strength and tensile strength from the experiments, a constitutive equation for the elastic–plastic nonlinearity of the welded joint was fitted with the Ramberg–Osgood equation.

By combining experimental data and welding properties, a finite element model of the wheel–rail contact in the welded joint of the large azimuth track was established. The global stress field distribution under different design loads was obtained through simulation, and the weak points under the ordinary working condition, start-up conditions, and braking conditions were determined, providing a theoretical basis for the health monitoring of the track and research on wear and damage.

Author Contributions: Conceptualization, X.C., H.L. and Q.X.; methodology, X.C.; software, R.Y.; validation, X.C., R.Y. and Z.Y.; formal analysis, Z.Y.; investigation, X.C.; resources, H.L.; data curation, Z.Y.; writing—original draft preparation, R.Y.; writing—review and editing, H.L.; visualization, R.Y.; supervision, Q.X.; project administration, H.L. and Q.X.; funding acquisition, H.L. and Q.X. All authors have read and agreed to the published version of the manuscript.

Funding: This research was funded by the National Key Research and Development Program of China, grant number 2021YFC2203600.

Data Availability Statement: The data presented in this study are available on request from the corresponding author. The data is not publicly available.

Acknowledgments: We thank the 39th Research Institute of China Electronics Technology Group Corporation for providing the weldment.

Conflicts of Interest: The authors declare that they have no conflicting financial interests.

References

1. Antebi, J.; Kan, F.W. Precision continuous high-strength azimuth track for large telescopes. In *Future Giant Telescopes*; SPIE: Avenue de l'Entreprise, France, 2002; pp. 612–623.
2. Anderson, R.; Symmes, A.; Egan, D. *Replacement of the Green Bank Telescope Azimuth Track*; International Society for Optics and Photonics: San Francisco, CA, USA, 2008; p. 784807.
3. Symmes, A.; Robert, A.; Dennis, E. Improving the service life of the 100-meter green bank telescope azimuth track. In *Ground-Based and Airborne Telescopes II*; SPIE: Avenue de l'Entreprise, France, 2008; p. 701238.
4. Juneja, G.; Kan, F.W.; Antebi, J. Update on slip and wear in multi-layer azimuth track systems. In *Optomechanical Technologies for Astronomy*; SPIE: Avenue de l'Entreprise, France, 2006; p. 627318.
5. Kumar, N.; Arora, N.; Goel, S.K. Weld joint properties of nitrogen-alloyed austenitic stainless steel using multi-pass GMA weld. *Archiv. Civ. Mech.* **2020**, *20*, 82. [[CrossRef](#)]
6. Han, P.; Wang, K.; Wang, W.; Ni, L.; Lin, J.; Xiang, Y.; Liu, Q.; Qiao, K.; Qiang, F.; Cai, J. Microstructure evolution and mechanical properties of Ti-15-3 alloy joint fabricated by submerged friction stir weld. *Archiv. Civ. Mech.* **2024**, *54*, 1–15.
7. Saranath, K.M.; Ramji, M. Local zone wise elastic and plastic properties of electron beam welded Ti-6Al-4V alloy using digital image correlation technique. a comparative study between uniform stress and virtual fields method. *Opt. Lasers Eng.* **2015**, *68*, 222–234. [[CrossRef](#)]
8. Zhang, Z.; Pan, B.; Grédiac, M.; Song, W. Accuracy-enhanced constitutive parameter identification using virtual fields method and special stereo-digital image correlation. *Opt. Lasers Eng.* **2018**, *103*, 55–64. [[CrossRef](#)]
9. Zhang, L.; Min, J.; Wang, B.; Lin, J.; Li, F.; Liu, J. Constitutive model of friction stir weld with consideration of its inhomogeneous mechanical properties. *Chin. J. Mech. Eng.* **2016**, *29*, 357–364. [[CrossRef](#)]
10. Tan, Y.; Shi, J.; Liu, P.; Tao, J.; Zhao, Y. Research on the Mechanical Performance of a Mountainous Long-Span Steel Truss Arch Bridge with High and Low Arch Seats. *Buildings* **2023**, *13*, 3037. [[CrossRef](#)]
11. Xu, L.; Li, Z.; Zhao, Y.; Yu, Z.; Wang, K. Modelling of vehicle-track related dynamics: A development of multi-finite-element coupling method and multi-time-step solution method. *Veh. Syst. Dyn.* **2022**, *60*, 1097–1124. [[CrossRef](#)]
12. Arslan, M.A.; Kayabasi, O. 3-D Rail–Wheel contact analysis using FEA. *Adv. Eng. Softw.* **2012**, *45*, 325–331. [[CrossRef](#)]
13. Tellikivi, T.; Olofsson, U. Contact mechanics analysis of measured wheel-rail profiles using the finite element method. *Proc. Inst. Mech. Engineers. Part F J. Rail Rapid Transit* **2001**, *215*, 65–72. [[CrossRef](#)]
14. Kuminek, T.; Anioek, K. Methodology and verification of calculations for contact stresses in a wheel-rail system. *Veh. Syst. Dyn.* **2014**, *52*, 111–124. [[CrossRef](#)]
15. Tian, J.H.; Jing, G.Q.; Lu, X.X.; Xiao, K.; Zhang, H.R. The rolling contact research of three dimensional wheel-rail based on finite element analysis. *Mater. Sci. Eng.* **2019**, *657*, 012072. [[CrossRef](#)]
16. Fu, L.; Qian, H.L.; Fan, F.; Zhong, J.; Liu, G.X. Analysis on Wheel-Rail Contact of 65-m Radio Telescope. In Proceedings of the 2011 International Conference on Electric Technology and Civil Engineering (ICETCE), Lushan, China, 22–24 April 2011; pp. 107–110.
17. Yang, Z.; Deng, X.; Li, Z. Numerical modeling of dynamic frictional rolling contact with an explicit finite element method. *Tribol. Int.* **2019**, *129*, 214–231. [[CrossRef](#)]
18. *ISO 6892-1:2019*; Metallic Materials—Tensile Tests—Part 1: Test Method at Room Temperature. International Organization for Standardization: Geneva, Switzerland, 2019.
19. *ISO 6507-1:2005*; Metallic Materials-Vickers Hardness test—Part1: Test Method. International Organization for Standardization: Geneva, Switzerland, 2015.
20. Ramberg, W. *Description of Stress-Strain Curves by Three Parameters*; National Advisory Committee for Aeronautics: Washington, DC, USA, 1943.

Disclaimer/Publisher's Note: The statements, opinions and data contained in all publications are solely those of the individual author(s) and contributor(s) and not of MDPI and/or the editor(s). MDPI and/or the editor(s) disclaim responsibility for any injury to people or property resulting from any ideas, methods, instructions or products referred to in the content.